DEVELOPMENT AND VALIDATION OF AN ADDITIVELY MANUFACTURED TILT-WING ACTUATOR FOR A SUBSCALE EVTOL DEMONSTRATOR

L. Ott*, M. May*, D. Milz*

* Institute of Flight Systems, German Aerospace Center (DLR), 82234 Weßling, Germany

Abstract

To support ongoing research into flight dynamics and control functions for (tandem) tilt-wing eVTOL aircraft, a subscale flight test demonstrator is being developed. Tilt-actuators are essential to achieve the tilt-wing's key characteristics of VTOL capability and efficient wing-borne cruise flight. However, these actuators must provide sufficient torque and speed to navigate the challenging transition regimes between cruise and hover flight, involving high angles of attack and post-stall conditions, with these requirements remaining poorly quantified. Additionally, existing solutions leave room for improvements in terms of weight and hardware accessibility. This work develops and validates a high-performance tilt-actuator system to enable comprehensive flight testing across a wide range of dynamic transition maneuvers. The maximum torque loads and tilt speed requirements of the tilt-actuators are derived. A primarily additively manufactured tilt-actuator and gear system leveraging commercial RC servo motors is developed, optimized, and implemented. The optimization analyses reveal that helical polymer gears are 2.7 times lighter than conventional metal spur gear alternatives while significantly reducing the package size. Bench tests successfully validate the static strength, accuracy, and dynamic performance of the optimized system, meeting all derived requirements.

Keywords

eVTOL Demonstrator; Additive Manufacturing; 3D printing; Tilt-Actuator; Tilt-Wing; TANDEMIC

1. INTRODUCTION

Electric Vertical Take-Off and Landing (eVTOL) aircraft enable advanced air mobility by eliminating reliance on runways, offering flexible transportation solutions for short-to-medium-range travel [1]. Electric propulsion systems have further expanded design possibilities, with tilt-wing configurations emerging as a leading approach to merge VTOL capabilities with comparably long range and high-speed cruise performance [2]. In addition, the tilt-wing architecture achieves hover efficiency below or equal to tilt-rotor configurations [3], with a more recent industry project¹ claiming better than tilt-rotor hover performance. However, the transition between hover and cruise flight introduces complex aerodynamic regimes with propeller-wing interactions and potential flow separation that demand sophisticated control systems to ensure stability [4, 5].

At the DLR Institute of Flight Systems, experimental validation of control laws is pursued with the **TANDEMIC** (Tilt-wing Aircraft for Novel Demonstrations of EVTOL Modeling and Innovative Control), a subscale tandem tilt-wing demonstrator. It features dual pivoting wings with Distributed Electric Propulsion (DEP), and is designed and built for wind tunnel and flight testing. This aircraft, shown in Figure 1, bridges the gap between theoretical models and real-world flight dynamics, partic-

ularly in validating novel control law approaches, estimated transition envelope boundaries, and failure mode responses [4,6].



FIG 1. Photo of the TANDEMIC

In the realm of possible eVTOL configurations, research has shown that, tilting and therefore sharing propulsion units between cruise and hover phases increases cruise efficiency [2]. This creates the need for lightweight and high-performance actuators to overcome the significant aerodynamic forces occurring during transition phases. This becomes especially relevant for tilt-wing aircraft where not only the rotors but also the wings are actuated. This trade-off between improved cruise efficiency and

¹https://acubed.airbus.com/blog/vahana/vahana-design-process-part-ii-preparing-for-lift-off/ [accessed Aug. 18, 2025].

increased actuator demands and complexity necessitates thorough analysis of these critical systems. For our research tilt-wing aircraft, these challenges are compounded by our goal to perform fast dynamic transition maneuvers that push the demonstrator aircraft to the edges of its capabilities.

1.1. State of the Art

Previous research tilt-wing aircraft have faced similar challenges and employed various solutions for their actuation needs. Notably, the NASA GL-10 demonstrator [7], a 26 kg aircraft with 3.17 m wingspan, uses an automotive linear actuator and lever arm system [8]. Flight testing of this system revealed shortcomings in terms of tilt speed and actuator torque, limiting the possible transition maneuvers and corridor [7], while also being deemed relatively heavy [8]. The later NASA LA-8 tandem tilt-wing demonstrator improved upon these issues by switching to a custom two-stage 20:1 metal gear system driven by an RC servo, which delivered comparable tilt speeds at or under 10 s to achieve a full 90° deflection and a 65% weight reduction, while achieving the same output torque of 40 Nm [8, 9]. This resulted in a 4.5% mass fraction of the LA-8's tilt-wing actuators relative to its take off mass [8,9]. Significantly lighter tilt-wing designs such as the SUAVI, a 4.46 kg quad tilt-wing UAV, were able to directly drive their wing tilt mechanism with an RC servo [10], presumably due to much lower torque requirements with smaller and slower flying systems. The TANDEMIC, with its 15 kg takeoff weight and 1.5 m wingspan, requires some form of gear reduction to work with commercial-off-the-shelf (COTS) servos to achieve sufficient torque.

1.2. Problem Statement

For small research teams, developing prototype aircraft comes with practical constraints including limited budgets, facilities, and timelines, which often preclude the expensive development and manufacturing typically needed for custom components. Additive Manufacturing (AM) offers a pathway to rapid prototyping of complex geometries, while COTS components (e.g., high-torque servos) provide cost-effective actuation solutions [11]. However, integrating AM and COTS elements into a tilt-wing actuator system presents significant challenges that demand careful optimization to balance and achieve:

- **Torque performance** (Overcoming the significant moment loads during the transitions)
- Dynamic performance (tilt speed, angular precision)
- **Structural robustness** (to guarantee safe operations)
- Weight minimization (to maintain overall aircraft weight and thrust-to-weight ratios)

The central research challenge thus becomes: How can a high-performance yet lightweight tilt-actuator system be designed and built to meet the torque and speed demands of research-focused transition flight while leveraging additive manufacturing and COTS components to minimize cost and development time.

1.3. Contribution

This study addresses this question through the development of a servo-driven actuator system for the DLR TANDEMIC, with a focus on:

- **Performance Requirements**: Estimating tilt speed and static and dynamic load requirements across the operational envelope (see Section 2).
- System Design: Optimization and comparison of 3D printed and metal gear sets (see Section 3).
- **Validation**: Experimentally validating structural integrity (see Section 4.1).
- **Performance Quantification**: Measuring the actuator's actual accuracy and dynamic performance (see Section 4.2).

Our methodology establishes transferable design principles for high-load actuation systems in transforming aerial vehicles, providing a framework that can be adapted to various eVTOL configurations requiring robust tilting capabilities under demanding aerodynamic conditions.

1.4. Key Parameters of the TANDEMIC Demonstrator

To provide sufficient context for the following analyses, a brief overview of the aircraft is listed in Table 1.

TAB 1. Key parameters of the TANDEMIC

Parameter	Value		
Configuration	Tandem tilt-wing		
Scale	pprox 1/4 of single-passenger aircraft ²		
Wingspan	1.5 m		
Design take-off mass	15 kg		
Cruise speed	28 m/s		
Wing area: aft / front	$0.335m^2/0.237m^2$		
Wing area: total	$0.572 \ m^2$		
Wing chord: aft $/$ front	$215mm\ /\ 157mm$		
Airfoil	GA(W)-1		
Max. flight loading	3G		
Propulsion system 8 motors & propel			
Thrust to weight ratio	(T/W) = 2		

2. ACTUATOR PERFORMANCE REQUIRE-MENTS

Accurate determination of aerodynamic loads is critical for designing a tilt-wing actuator capable of operating throughout the full transition envelope. This section derives the torque and tilt-speed requirements for the TANDEMIC tilt-wing actuator system, with emphasis on the transition phases under normal and boundary flight conditions.

²Inspired by the Airbus A³ Vahana: https://acubed.airbus.com/projects/vahana/ [accessed Aug. 18, 2025].

2.1. Torque Requirements

The total torque requirement on the tilt-actuators is derived from the aerodynamic moments acting on the tilt-wings and the attached distributed electric propulsion system. Both worst-case scenarios and normal operational envelope boundaries are analyzed. This also ensures the tilt-wing actuators are structurally sized to handle and recover from significant failures during transitions.

2.1.1. Wing Moment Loads

The wing moments scale quadratically with airspeed and linearly with the moment coefficient that increases with Angle of Attack (AOA), making high-speed high-AOA transition maneuvers particularly demanding for the actuation system. NASA's GL-10 flight test report [7] documents these challenges, noting that maximum aerodynamic moments occur during high-speed inbound transitions (cruise to hover) while experiencing substantial airspeed. This primarily occurs in the high angle of attack range of 60° to 20° at speeds up to 40 kts (20.6 m/s) [7]. The TANDEMIC uses the GA(W)-1 airfoil for its wings, which has been extensively validated and provides solid empirical data in the literature. For this analysis, wind tunnel data for the GA(W)-1 airfoil covering the full 360° AOA range including deep stall conditions is utilized [12]. No propeller slipstream was applied in this study, which can be neglected at the beginning of an inbound (decelerating) transition, where airspeed is high and thrust is low. The aerodynamic moments acting on each wing are calculated using the standard equation:

(1)
$$M = \frac{\rho}{2} \cdot S_{ref} \cdot V^2 \cdot l_{\mu} \cdot C_m$$

where ρ is air density (1.225 kg/m^3), S_{ref} is the reference wing area , V is airspeed, l_{μ} is the reference wing chord length and C_m is the moment coefficient.

Figure 2 shows the moment coefficient behavior, which continues to increase in magnitude beyond the stall point (approximately 16° AOA), reaching maximum values of -0.6 around 115° angle of attack before decreasing at higher angles. We view AOAs above 60° as outside the normal operational envelope of our demonstrator aircraft. These values are therefore only relevant for failure recovery and worst case scenarios.

The TANDEMIC also incorporates elevon control surfaces that can affect the maximum aerodynamic moments during transition, especially during runaway failure scenarios. Wind tunnel tests of similar configurations [13] show that flap effectiveness decreases significantly at high angles of attack due to flow separation. However, distributed electric propulsion effects alter this behavior. Existing studies suggest that the propeller slipstream can reintroduce some control surface effectiveness even at higher angles of attack around 60° [14]. Therefore, for a worst case scenario, the δC_m at full effectiveness is taken into account and added to the total C_m acting on the wing and actuator. With the flap chords being 26.5% and 36.3% and the flap lengths being 370 mm



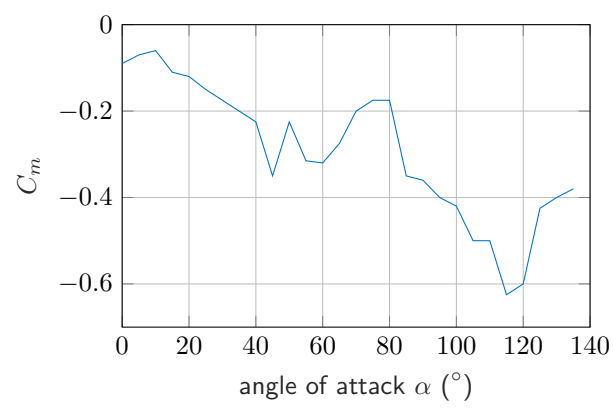


FIG 2. C_m Wind tunnel data GA(W)-1 airfoil at Re=0.37e6; taken from [12]

or about 50% of the wingspan, at maximum elevon deflection $\eta_{max}{=}30^\circ$ we get $\delta C_{m\eta}=$ -0.067. This is using standard calculation formulas with empirical correction factors [15, p. 435-445] derived from wind tunnel data of the GA(W)-1 airfoil [16]. The worst-case AOA range is set from -45° to 135°, including significant pitching angles of \pm 45° on top of the wing tilt angles. This results in a absolute worst-case C_m of -0.687 at 115° AOA with symmetric full flap deflection.

To find the maximum moment loading, the maximum airspeed at which transitions can be safely performed must be determined. The TANDEMIC demonstrator and its wing structures are sized for 3G loading conditions. With these boundary conditions, a maximum safe airspeed of 25.5 m/s is determined, which always guarantees a wing loading under 3G even at 90° AOA. For AOAs up to 30°, the maximum safe airspeed exceeds the cruise speed of 28 m/s, permitting even fairly aggressive inbound transitions from cruise speed to hover. To manage the worst-case $C_m =$ -0.687, the actuators need to handle 19.7 Nm at the aft wing and 10.2 Nm at the front wing. This represents the extreme upper end of AOA and speed combinations, that should only occur during failed transitions where the aircraft might temporarily lose control. As previously mentioned, we estimate our upper operational AOA boundary to be at 60° with little to no elevon deflections at higher speeds. This leads us to a $C_m =$ -0.4, which at the save maximum airspeed of 25.5 m/s yields 11.5 Nm and 5.9 Nm, respectively. These values comprise the maximum wing moment load under normal operational conditions.

2.1.2. DEP Moment Loads

3

The moments imparted by the propellers of the DEP system need to be considered as well. Windtunnel tests reported by Simmons [17] show that propellers on vectored thrust eVTOLs such as tilt-wings exhibit pronounced off axis forces and moments across the broad spectrum of operating points encountered during vertical to horizontal transition. These moments that also act around the pitch axis become especially relevant when the propulsion system is commanded to high wing-tilt and therefore high

©2025

propeller incident angles in the transition regime [18]. These wind tunnel tests show moments acting in the tilt axis of up to $0.5 \, \text{Nm} \, (0.38 \, \text{ft-lbf})$ measured at $21.64 \, \text{m/s}$ (71 ft/sec) and 45° to 50° incident angles with a single three-bladed 16-inch diameter, 8-inch pitch propeller at $\approx 6000 \, \text{rpm}$ [18]. The TANDEMIC uses two-bladed 16-inch diameter, 6.1-inch pitch propellers, which should result in comparable or lower moments at the same inflow conditions due to the lower pitch and rotor solidity [17]. It was observed that higher free-stream velocities resulted in higher moments [18]. Therefore, we assume that the higher velocity of 25.5 m/s should roughly equal out the aforementioned diminishing factors, and we take the 0.5 Nm as our best guess value for the maximum aerodynamic moment induced by each propeller acting in the actuator axis, totaling an additional 2 Nm per wing.

This brings the total required torque due to aerodynamic moments for realistic transition profiles to 13.5 Nm for the aft wing and 7.9 Nm for the front wing. This does not include the dynamic torque needed to overcome the rotational inertia of the tilt-wings, which, depending on the angular acceleration, can be significant. Therefore, the final actuator torque should provide sufficient overhead (based on measurements of our finished actuator hardware the angular acceleration reaches 400 to $800^\circ/s^2$, depending on the amplitude of movement, requiring 5 to $10~\mathrm{Nm})$

2.2. Tilt-Speed Requirements

As described in the state-of-the-art section 1.1, the tilt speed of the actuators can be a limiting factor for the possible transition profiles that can be achieved To further quantify this issue, we employ our optimal-control-based approach established in prior work [19] to assess the effects of various constraints on the tilt-actuators' dynamic performance. With this approach, we can directly optimize for the shortest possible transition profile and identify the theoretical limits of the aircraft's dynamics and derive a tilt-speed requirement to match those boundaries if at all feasible. The transition is simulated using a 3DOF aero-propulsive model. Our implementation allows setting a time constant and an angular rate constraint for the actuators, which enables a progressive actuator performance decrease to gauge the effects on total transition times. The analyses examine both outbound transitions (hover to cruise) and inbound transitions (cruise to hover), with the aircraft's pitch locked in a horizontal attitude for both cases.

Table 2 summarizes the transition time analyses, starting with a rate constraint that is typical of an COTS RC servo motor in a "direct drive" scenario without additional gearing of $550\,^\circ/\text{s}$ (data sheet value of the COTS servo at hand). Subsequent analyses increase the gear reduction ratio to 8:1, 32:1 and 64:1, reducing the maximum rate of the simulated actuator accordingly. The transition trajectory optimizations will either be kept at the same height, hereafter called a level transition or be unconstrained in that regard, referred to as a free transition.

TAB 2. Transition times - overview

Gear	Rate	90°	Out-	In-	Comment
Ratio	Cons. (°/s)	Tilt (s)	bound (s)	bound (s)	
1:1	550	0.16	2.7	4.3	Level/Free
1:1	550	0.16	1.7*	14.0	Level/Level
8:1	68.75	1.3	3.4	16.3	Level/Free
32:1	17.19	5.2	6.2	38.6	Level/Free
64:1	8.59	10.5	10.6	60.1	Level/Free

Note: *Variable blade pitch scenario, no thrust decline

For the 1:1 case, the time constant that is applied to the tilt-angle change is kept at a minimum of 0.1s, since lower values resulted in local minima in the transition time. Further constraints ensure a level transition maneuver, so height changes are kept to a minimum. With these boundary conditions, the following results shown in Figure 3 are obtained, where u is the horizontal speed, x is the covered horizontal distance, T is the thrust, and δ_w is the wing angle. The subscripts 1 and 2 refer to the aft and front wing, respectively.

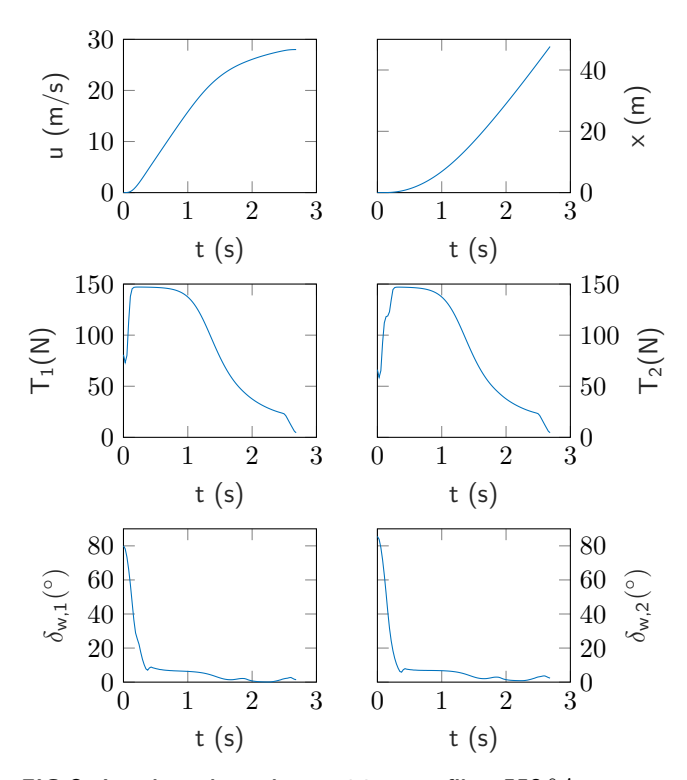


FIG 3. Level outbound transition profile, 550 $^{\circ}/s$ constraint

The results shows a quick tilt movement at the beginning combined with high thrust levels that later taper off due to the inflow velocity reducing the maximum available thrust. This is due to the fixed-pitch propellers' inability at certain inflow velocities to generate the maximum thrust when the upper RPM limit of the propellers is reached. In the simulation, this is implemented via a simple model subsequently reducing the maximum thrust available after a critical advance ratio. This yields a min-

©2025

imum transition time of $2.7\,\mathrm{s}$. This thrust decline could be greatly reduced by implementing variable blade pitch propellers, which in an ideal scenario without any decline up to $28\,\mathrm{m/s}$ would yield a minimum transition time of $1.7\,\mathrm{s}$. The former and further results on the transition profiles can be found in the Appendix.

For context on how quickly an inbound level transition would unfold with such actuator constraints, Figure 4 depicts how the aircraft could transition back to hover in 14s. The aircraft shows some interesting behavior from about 4s into the maneuver where deceleration seems to nearly halt, suggesting the aircraft struggles to move through this region while also keeping the z height constant. Though it must be noted that the current simulation does not incorporate the elevons of the aircraft that could provide the additional control authority needed to overcome this deceleration barrier.

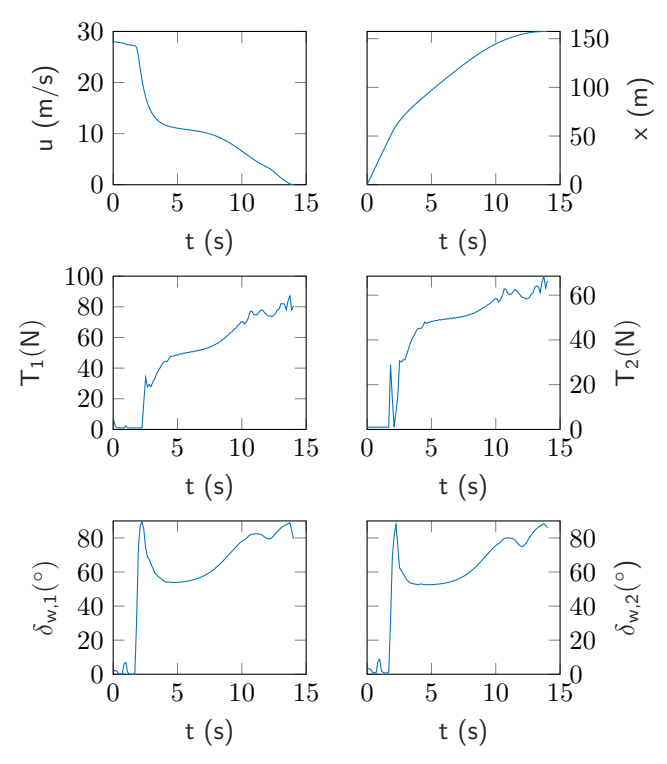


FIG 4. Level inbound transition profile, $550^{\circ}/s$ constraint

Removing the z height constraint gives an inbound transition time of $4.3 \, \text{s}$, where the aircraft is continuously able to decelerate by trading kinetic with potential energy. In the case of the outbound transition, a slight decrease of $0.1 \, \text{s}$ to $2.6 \, \text{s}$ total was observed.

Adding an 8:1 reduction to the servos scales the rate constraint accordingly to 1/8 or $68.75\,^{\circ}/s$, which is equivalent to a 90° tilt time of about $1.3\,\mathrm{s}$. The time constant is also increased to $0.2\,\mathrm{s}$, taken from our measurements. This increases the level outbound transition time to $3.4\,\mathrm{s}$; the level inbound transition shows the same deceleration limit behavior, so this case will no longer be looked at. The free inbound transition takes significantly longer with these constraints resulting in a total time of $16.3\,\mathrm{s}$.

A further quadrupling of the gear ratio to 32:1, with a $17.19^{\circ}/s$ rate constraint and a 5.2s tilt time, yields 6.2s for the level outbound case and 38.6s for the inbound

transition, continuing the trend that the inbound transition time is much more sensitive to actuator speed than the outbound one.

Increasing the gear ratio to 64:1 with an $8.59\,^\circ/s$ rate and $10.5\,s$ tilt time reveals $10.6\,s$ for the level outbound case, which neatly shows how at this stage the time is essentially limited by the actuator speed. The inbound transition ends up at $60.1\,s$.

3. GEAR SYSTEM DESIGN AND OPTIMIZA-TION

With the torque requirements set and the context on how tilt speed affects transition times, the actuator itself can be designed and optimized while staying compact, lightweight, and robust. For the TANDEMIC, the decision was made to use the same actuator design for the aft and front wing to reduce complexity and to achieve similar tilt-speed characteristics. Therefore, the following analyses focus on the aft wing actuator since it is the one that experiences the higher loading. To drive the actuator, a high-power 8.4 V RC servo was chosen with the specifications in Table 3, which provided a good balance of torque, speed, and affordability.

TAB 3. Specifications for Savöx SB-2290SG Servo Motor

Parameter	Value
Name	Savöx SB-2290SG
Maximum speed	$545^{\circ}/s$ @ $8.4V$
Torque (Stall value)	6.9 Nm @ 8.4 V
Torque (Running value)	2.6 Nm @ 8.4 V
Weight	81 g
Dimensions $(L/W/H)$	$40.3/\ 20.2/\ 38.7\ mm$

To achieve the desired output torque and speed with the given servo, an 8:1 gear ratio was chosen as a balance of high torque output of up to 20.8 Nm, which should provide ample dynamic margin in addition to the required 13.5 Nm to overcome the maximum operational aerodynamic moments as well as losses in the gears and bearings. It is also beneficial to not operate the servo near its torque limit since the speed at which it can generate said torque decreases with load. This should provide sufficient speed even under medium load, with a theoretical tilt time of 1.7 s and a rate constraint of $\approx 70^{\circ}/\text{s}$, effectively allowing outbound transition times down to 3.4 s and inbound transitions down to 16.3 s. If future flight tests reveal too conservative torque overhead, the gear ratio can be reduced to increase max. speed instead.

To create the actual gear hardware, the aim is to leverage additive manufacturing using polymers and standard desktop machines to shorten development cycles and make custom gearing readily available to a small research team. Concerning the durability of the available 3D printing materials for application in gears, the literature shows promising cycle lives of 10^5 to 10^6 depending on the loading and materials used [20,21]. The application in a tilt-wing mechanism may be uniquely suited from a durability standpoint, since the loading is not con-

©2025

tinuous, reducing heating effects which can reduce the lifetime significantly [20]. To put these numbers into perspective, a tilt-wing aircraft like the TANDEMIC with a flight time of about $0.5\,\mathrm{h}$ for a single eVTOL flight with two transitions could theoretically fly continuously for 2.9 years before hitting 10^5 tilt cycles and 29 years for a 10^6 limit. In any case, using it in the prototype application of a research vehicle, the long-term durability should not be a concern.

A further common concern regarding polymers is their strength and stiffness, though as shown in Table 4, in terms of specific strength, these materials at least provide values in a similar order of magnitude or even slightly better compared to metals like aluminum or stainless steel, especially in bending load cases.

TAB 4. Material properties and specific strength

Material	Density	Tensile/ Flexural Strength	Specific Strength
Symbol	ρ	$\sigma_{\sf max}$	
Unit	(g/cm^3)	(MPa)	(MPa·cm ³ /g)
PEEK [22]	1.32	116/175	87.9/132.6
ULTEM 1010 [22]	1.27	80/—	63.0/—
PPS-CF ³	1.26	87/142	69.0/112.7
Polycarbonate (PC) ⁴	1.20	62/108	51.6/90
SAE 304 [22]	7.93	515/205	64.9/25.9
Al 6061 T6 [22]	2.71	290/240	107.0/88.6
Inconel 718 [22]	8.19	1240/1034	151.4/126.3

Where polymers show larger deviations from metals is with their specific modulus values, which are an order of magnitude to 1/4 the value of metals. Though in a geared application, this might even prove beneficial since the pressure contact stresses that are one of the governing factors are reduced proportionally to the modulus of the material [23, p.341].

To build a compact and lightweight gear set, the geometric design freedom of additive manufacturing, in our case standard Fused Filament Fabrication (FFF), shall be employed to create custom and optimized helical gears. These provide reduced loading and smoother operations since the helical angle allows contact ratios greater than two, meaning the minimum amount of teeth that are in contact with each other is always greater than two [23, p.352]. This effectively halves the stresses experienced by the gear teeth and therefore allows much more efficient

structures [23, p.352]. This also comes with drawbacks; the helical angle introduces axial side forces which need to be managed, though this can be elegantly solved by a symmetric side-to-side arrangement of the gear teeth angles, alleviating the stresses inside the gears themselves [23, p.354]. This arrangement in turn makes the manufacturing via conventional methods more difficult and expensive [23, p.354], which is not an issue with additive manufacturing processes.

This opens up the possibility to optimize the set of free dimensions that creates the lightest gear set, given certain geometrical and material constraints. This is implemented using the interior-point gradient-based optimization algorithm commonly used for engineering applications (MATLAB optimization toolbox; fmincon). To avoid local minima, a grid search of the optimization's starting values was added. The gear dimensions and resulting stresses are calculated using standard textbook formulas [23], constrained to below the allowable levels, and a gear set volume and weight are calculated to be subsequently minimized. To assess the performance of polymers in such a geared application, the same optimization is run with the material characteristics of representative metals, and the weights are to be compared. A further comparison shall be between helical and standard spur gear geometries. Assessing the potential weight reduction of the former and the potential advantage additive manufacturing provides in incurring no additional costs to create the required intricate geometries. The last comparison will be one between single and two-stage gear systems, to avoid disadvantaging one or the other due to the chosen gear ratio of 8:1.

3.1. Gear Optimization Methodology

The optimization process employs a constrained nonlinear minimization approach to determine the lightest possible gear set while satisfying all structural and operational constraints. The objective function minimizes the total mass of the gear set, calculated as the product of volume and material density.

The structural integrity of the gear set is verified through comprehensive stress analysis. Tooth root stresses are calculated following standard gear design methodology as described by Hinzen [23], with appropriate safety factors applied to ensure reliability under operational loads.

An additional stress constraint was implemented beyond standard tooth calculations. Without this, the optimization would unrealistically increase gear width to reduce tooth stresses, creating geometries that would fail due to shaft deformation and torsion under operational loads. The following stress components experienced by the pinion gear shaft are considered:

- Shear stress: Inside the pinion shaft due to the torque and radial forces.
- Bending stress: A conservative approach is used where the pinion is modeled as a 3-point beam with a single concentrated radial load at mid-span.

The stress state in the pinion shaft is then evaluated using the von Mises criterion. This equivalent stress is then compared against the material's yield strength with an

©2025

³Material properties for PPS-CF from Technical Data Sheet, available at: https://store.bblcdn.eu/s8/default/623b28bf2fbe495 fa9dd559a85f494ed/Bambu_PPS-CF_Technical_Data_Sheet.p df [accessed Aug. 18, 2025].

⁴Material properties for PC from Technical Data Sheet, available at: https://store.bblcdn.eu/s8/default/ab03007d58814bc 28a08145719b552de/Bambu_PC_Technical_Data_Sheet.pdf [accessed Aug. 18, 2025].

appropriate safety factor. The implemented constraints ensure a physically realizable design that maintains structural integrity (though not all effects of very wide gears are captured; this should balance the optimization towards more feasible gear designs).

3.2. Structural Constraints

The optimization incorporates the following structural constraints with safety factor SF = 1.5:

 $\begin{array}{ll} \bullet \ \ {\rm Tooth\ root\ strength:} & \sigma_{\rm mises} \cdot SF \leq \sigma_{\rm max} \\ \bullet \ \ {\rm Hertzian\ contact\ pressure:} & \sigma_{\rm hertz} \cdot SF \leq p_{\rm max} \\ \bullet \ \ {\rm Pinion\ shaft\ integrity:} & \sigma_{\rm mises\ pinion} \cdot SF \leq \sigma_{\rm max} \\ \end{array}$

• Contact ratio: $e_{\gamma} \geq 1$

• Single-stage clearance: $a_1 \geq r_{\rm pinion} + r_{\rm bracket}$ • Two-stage clearance: $a_2 \geq r_{\rm inter} + r_{\rm WS} + 2$ mm

The constraints cover the stresses experienced by the gears as well as a minimum contact ratio greater than one to ensure feasible gear meshing geometries. The additional clearance constraints ensure that the relevant pinion and intermediate gears $(r_{\rm pinion}, r_{\rm inter})$ have sufficient spacing (a_1, a_2) and do not physically interfere with the bracket of the main gear $(r_{\rm bracket})$ or the wing spar tube $(r_{\rm WS})$.

3.3. Material Selection

Five candidate materials were evaluated, with properties in Table 5, sorted by their modulus. Three 3D printing materials were chosen that can be fabricated using standard non-industrial grade FFF 3D printers, Polycarbonate, Greentec Pro, and PPS-CF, with increasing Young's modules. They were also chosen for their good mechanical and heat resistance properties. Aluminum 6061 T6 and Inconel 718 were chosen to represent light and heavyduty metals, to serve as the performance comparison against the polymers.

TAB 5. Material properties for gear candidates

Property	PC	GT Pro	PPS- CF	AI 6061	Inconel 718
$\sigma_{\sf max}$ (MPa)	55	58	87	276	1100
$p_{\sf max}$ (MPa)	55	58	87	441	1760
$E\ (MPa)$	2110	4300	8230	69e3	193e3
$ ho$ (g/cm 3)	1.20	1.35	1.26	2.70	8.13
Cost (€/kg)	43	60	178	-	-

For the maximum allowable contact pressure $p_{\rm max}$, a multiplier of 1.6 of the maximum tensile yield stress was used for the metals based on literature [24, p. 779], though this is a best-guess estimate and other approaches to determine this from available material data were found while researching. For the polymer materials, no such multipliers were found, and to stay conservative and to lower the chance of excessive friction damaging the gear teeth, the tensile yield stress was taken without a multiplier. This uncertainty is one of the weaknesses in terms of accuracy of the following analyses. A further compromise was made in the selection of the maximum allowable tensile yield stress of the 3D printed materials since with

the chosen layered FFF fabrication process, the material properties are anisotropic and generally weaker between the layers. For the analyses, the tensile yield strength in the layer plane was chosen as a baseline, since most teeth loads occur in this direction.

3.4. Helical Gear Optimization Results

The first batch optimization run, which looks at the lightest gear set with helical teeth geometries, was conducted with the following bounds shown in Table 6.

TAB 6. Helical gear optimization parameter bounds

Parameter	Lower	Upper	Units	Description
m_n	0.5/1.0	4.0	mm	Normal module
N_{pinion}	8.0	30.0	-	Pinion teeth count
b_t	3.0	40.0	mm	Face width
β	0.0	45.0	0	Helical angle

Note: Bounds apply to both single stage and two stage configurations where applicable

For the two-stage optimization run, the stages are optimized as a system, and the gear ratio split between the two stages is free to move to achieve the total gear ratio of 8:1. The minimum teeth count for the helical gears was set to 8 [23, p. 350]. The lower bound of the normal module $m_{n,LB}$ is limited by the given manufacturing methods' ability to create small precise teeth. We choose $m_{n,LB} = 1$ mm, with its minimum tooth height of 2.25 mm as the lower limit for our FFF 3D printing process with a standard 0.4 mm nozzle. For metal gears manufactured via conventional cutting tools $m_{n,LB} =$ 0.5 mm with 1.125 mm tooth height was selected, though this could also be achieved via additive manufacturing with either FFF and a 0.2 mm nozzle (which comes with its own set of problems), or a different method like Stereo Lithography (SLA). With these boundaries and the constraints set in Section 3.2, the following results in Table 7 for the single and two-stage gear systems were obtained for each material. It can be observed that a single-stage system is always the lighter option with weight reductions between 3% to 17%.

TAB 7. Gear system mass comparison - Helical

Material	Single	Two	Best	Reduction
	(g)	(g)	Config.	(%)
PC	24.29	25.20	Single	3.6
GT Pro	28.69	34.09	Single	15.8
PPS-CF	25.63	28.08	Single	8.7
AI 6061	16.87	20.25	Single	16.7
Inconel	21.62	23.44	Single	7.7

Table 8 shows the weight results relative to each other, normalized to the best results for each staging scenario. This shows aluminum as the lightest material overall, fol-

lowed by Inconel. PC and PPS-CF are 44% and 52% heavier than the single stage aluminum reference.

TAB 8. Performance comparison against best results - Helical

Material	vs Best Single	vs Best Two	Min SF
	(%)	(%)	(-)
PC	44.0	24.4	1.50
GT Pro	70.1	68.3	1.50
PPS-CF	51.9	38.7	1.50
AI 6061	0.0	0.0	1.50
Inconel	28.2	15.8	1.50

Note: percentages show weight increase relative to the best result (0% = best); metals are shown with ($m_{n,LB}=0.5$)

To evaluate the space requirements of the gear systems within the aircraft, two gear set examples are analyzed relative to the wing spar tube dimensions. The single-stage result for the polycarbonate 3D printing material is shown in Figure 5.

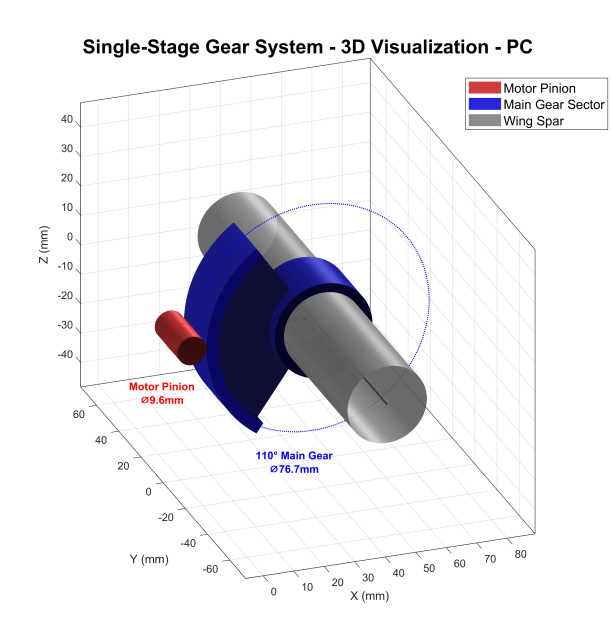


FIG 5. PC single stage helical gears

The two-stage result is shown in Figure 6. In both cases, the aft wing's spar tube is to scale and shows the length inside the fuselage between the tilt-wing bearings. The gears are shown with their pitch dimensions without rendering the teeth, but the width and the main gear's sector, disk, and bracket dimensions are captured correctly. Both examples show that the optimization for PC favors wide gears with 20 mm for the single stage and 22 mm for the two-stage system.

3.5. Spur Gear Optimization Results

With the context on the weight and package size needs of optimized helical gear systems, a comparison to more conventional spur gear geometries can be drawn. This should be more representative in the case of the metal materials of what could be fabricated or procured for

Two-Stage Gear System - 3D Visualization - PC

First Pinion Intermediate Gear Second Pinion Main Gear Sector

Wing Spar

Second Pinion Mini Gear Gear System - 3D Visualization - PC

First Pinion Intermediate Gear Second Pinion Main Gear Gear Gear Minion Main Gear Gear Gear Minion Gear Gear Gear Minion Gear Gear Gear Gear Minion Gear Gear Gear Gear Minion Gear Gear Minion Gear Gear Gear Minion Gear Gear Gear Minion Gear Minion Gear Gear Minion Gear Minion Gear

FIG 6. PC two stage helical gears

a research prototype or low production volume eVTOL unmanned aerial system (UAS) with reasonable costs. The spur gear optimization was conducted with the following bounds shown in Table 9.

TAB 9. Spur gear optimization parameter bounds

Parameter	Lower	Upper	Units	Description
m_n	0.5/1.0	8.0	mm	Normal module
N_{pinion}	9.0	60.0	-	Pinion teeth count
b_t	3.0	40.0	mm	Face width
β	0.0	0.0	0	Helical angle

Note: Bounds apply to both single stage and two stage configurations where applicable $\,$

The minimum tooth count was now set to 9, as a minimum for spur gears [23, p. 343]. The helical angle was bound to be always zero, forcing a spur gear geometry. This yielded the results in Table 10, which shows significantly higher weights compared to the helical case, for both the single-stage as well as the two-stage setups with the former being around 20% lighter.

TAB 10. Gear System Mass Comparison - Spur

Material	Single	Two	Best	Reduction
	(g)	(g)	Config.	(%)
PC	106.42	134.90	Single	21.1
GT Pro	214.28	264.72	Single	19.1
PPS-CF	169.39	209.02	Single	19.0
AI 6061	118.81	146.15	Single	18.7
Inconel	66.34	80.61	Single	17.7

Table 11 again shows the relative weights for each staging scenario.

©2025

TAB 11. Performance comparison against best results -

Material	vs Best Single	vs Best Two	Min SF
	(%)	(%)	(-)
PC	60.4	67.4	1.50
GT Pro	223.0	228.4	1.50
PPS-CF	155.3	159.3	1.50
AI 6061	79.1	81.3	1.50
Inconel	0.0	0.0	1.50

Note: percentages show weight increase relative to the best result (0% = best); metals are shown with ($m_{n,LB} = 0.5$)

Here much higher variation is present compared to the helical analyses, with Inconel being the lightest in both staging categories, followed by PC.

Looking at the spur gear package size needs exemplified by the polycarbonate two-stage system shown in Figure 7 one can see that it is five times as large in terms of main gear diameter as even its single-stage helical version with 379.1 mm vs 76.7 mm, rendering it too large to integrate it into the aircraft's fuselage. For the Spur gears only the Inconel variants would be small enough in size to be implementable. The other materials would need an additional maximum size constraint to produce viable flight hardware.

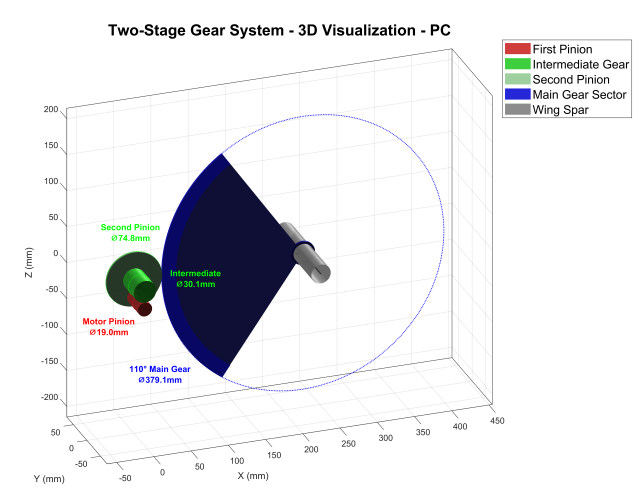


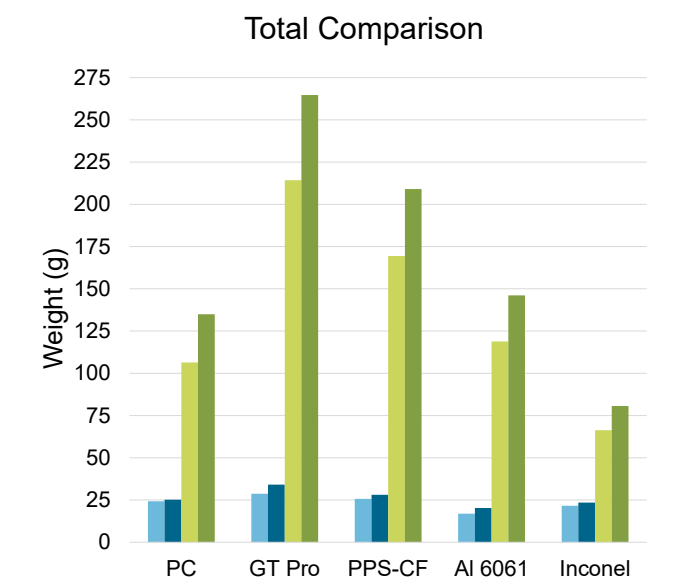
FIG 7. PC two stage spur gears

3.6. Comparison of Helical vs Spur Gears

With the data on the optimized weights for each material, staging count, and teeth geometry, an in-depth comparison can be drawn. Figure 8 shows an overview of the absolute weights of each gear set.

The relative weight reduction of helical vs. spur gears can be seen in Table 12. The reduction magnitude on average is in the 70 - 85% range, with Inconel benefiting the least.

Table 13 is showing the relative weight difference between single stage 3D printed polymer-based helical gears against the lightest metal spur gears. We view this as



■ Helical Single (g)■ Helical Two (g)■ Spur Single (g)■ Spur Two (g)FIG 8. Helical vs spur gear bar chart weight comparison

TAB 12. Helical vs Spur gear weight comparison - Percentage reduction

Material	Single Stage	Two Stage	Avg. Re- duction
	(%)	(%)	(%)
PC	77.2	81.3	79.2
GT Pro	86.6	87.1	86.9
PPS-CF	84.9	86.6	85.7
AI 6061	85.8	86.1	86.0
Inconel	67.4	70.9	69.2

the most relevant comparison for our application in the aircraft, since custom helical metal gears would be cost-prohibitive, and spur gears in contrast could be procured as COTS components. Here one can see that the polymers paired with optimized helical gear geometries enabled by additive manufacturing significantly outperform their metal spur gear counterparts by factors of 2.3 - 4.9x. Polycarbonate is leading the polymers in weight reduction with being 2.7x lighter than the best metal spur gear made from Inconel.

TAB 13. Helical polymer vs spur metal references

3D Print	Weight		Reduction	
	Savings (%)		Factor	•
Material	vs Al	vs Inconel	vs Al	vs Inconel
PC	79.6	63.4	4.9x	2.7x
GT Pro	75.9	56.8	4.1×	2.3x
PPS-CF	78.4	61.4	4.6x	2.6x

Al Spur Ref: 118.81g, Inconel Spur Ref: 66.34g; $\mathbf{m}_{n,LB}=0.5$

These weight reductions are achieved in light of a scenario where both the additively manufactured helical gears and metal spur gears are optimized, which for the latter might

not be as easily realized if one needs to find and procure COTS metal gears that may not closely match the optimum specifications.

To summarize, the optimized helical gear geometry successfully balances mass minimization with structural integrity and allows lightweight and compact single and two-stage gear sets. This results in helical gears made from polymers that are 44 - 70% heavier than their helical metal counterparts when the later are taking advantage of smaller feasible tooth heights and modules. Compared to conventional metal spur gears the additive manufactured polymer helical gears are significantly more compact and up to 2.7 times lighter, making them the obvious choice for our application, while being readily accessible via FFF 3D printing and very cost effective with material costs in the 1 - 3.5€ range per gear set.

4. ACTUATOR BUILD AND VALIDATION

The actuator and helical gear system that is implemented in the TANDEMIC as of writing is a version that has been optimized and designed with an older version of the optimization methodology presented in this paper and therefore does not use the lightest possible 3D printed gear set and material that was found in the previous detailed analyses. It uses the Greentec Pro material, chosen at the time for its high temperature resistance and modulus. It is built using a single-stage setup, for weight and complexity reductions vs a two stage setup. The gear set has the following specifications shown in Table 14.

TAB 14. Single-Stage Gear System - Hardware

Parameter	Value
Actuator system overview	
Optimized gear set mass	61 g
Total actuator mass	295 g
Gear ratio	8.0
Overall min safety factor	2.2
Required safety factor	1.5
Gear specifications	
Transverse Module	1.5 mm
Pinion Teeth	8
Main Gear Teeth	64
Face Width	30.0 mm
Helical Angle	35.0°
Pinion Diameter	12.0 mm
Main Gear Diameter	96.0 mm

An image of the 3D printed hardware implemented into the aft fuselage structure of the aircraft can be seen in Figure 9. The tilt-wing angle is transmitted via a separate small 1:1 gear set that is mounted on the left bracket into the axis of the servo and transferred via a small connecting rod through the center hole of the pinion gear onto the built-in sensor (potentiometer) of the servo. A newer iteration of the assembly also includes an auxiliary



FIG 9. Actuator hardware built into the aft structure

magnetic encoder positioned beside the supporting gear to accurately measure the tilt angle.

4.1. Structural Validation

To validate the stress calculations and assumptions of the optimization process, static load tests until failure were performed. To create the necessary moments, a lever arm was connected to the tilt wing spar tube and subsequently loaded with increasing weight to determine the failure moment. During these tests, the servo was removed and the pinion gear was prevented from turning at the servo interface, matching the loading scenario the gears would see under operational conditions. The test showed no failure or permanent deformation up to a 36 Nm load, which equals a safety factor of 1.7 when applied to the 20.8 Nm maximum output torque of the actuator and 2.7 in reference to the maximum expected aerodynamic load of 13.5 Nm. At the next loading step of 38.5 Nm, the pinion gear failed with a brittle fracture near the middle of the width. This indicates reasonable assumptions and stress calculations for at least one of the 3D printing materials and optimized designs (multiple specimens were tested with same or better results), though for a full validation of the optimization results, more experiments with different designs and materials would need to be conducted.

To validate the servo's ability to move the tilt-wing with reasonable speed under high load scenarios, a dynamic test was conducted where the actuator was loaded via the same lever arm setup with 18 Nm and was signaled to perform a movement from -15 $^{\circ}$ to +15 $^{\circ}$ against the horizontal line to keep the moment load of the weight acting on the lever arm more or less constant. This resulted in a 1s tilt time for a 30° movement that also had to overcome the significant rotational inertia of the lever arm and weight. Therefore, a sub-3s tilt time for a 90° movement is assumed even under very high loads. This also doubled as a test of the helical gears' ability to handle additional dynamic loading torques (due to inertial resistance) even under very high base load, mimicking the loading in the turbulent post-stall flow conditions of high-speed inbound transitions.

4.2. Dynamic Performance Characterization

To quantify the actuator's dynamic performance, the following tests were conducted to identify the actuator's behavior.

- Tracking accuracy tests: Tracking of a linear command through the full tilt range to measure the accuracy and linearity.
- **Step tests**: to identify the step response, time constant (63% of final value), and the precision in hitting the requested angle.
- Hysteresis test: to quantify the hysteresis of the actuator when sweeping up or down at different speeds and angle ranges.
- Tracking bandwidth test: to quantify the tracking behavior, where amplitude and phase of the tilt-angle are measured with increasing sinusoidal input frequencies, again over different angle ranges.

All of the tests were performed without external moment loads, aside from the inertial load of the fully integrated aft tilt wing. For the measurements, a microcontroller was programmed to perform the various test routines, sending out pulse width modulation (PWM) signals to the tilt servo and sampling the magnetic angle encoder (14-bit resolution: 0.0219°) at 50 Hz for all measurements besides the bandwidth measurements, which were done at 100 Hz. Throughout all tests, the servo and its built-in controller and angle sensor were handling the position control of the tilt angle.

4.2.1. Tracking accuracy tests

A linear sweep over the full tilt range was performed over a 60 s duration, showing the following result measured via the encoder in Figure 10.

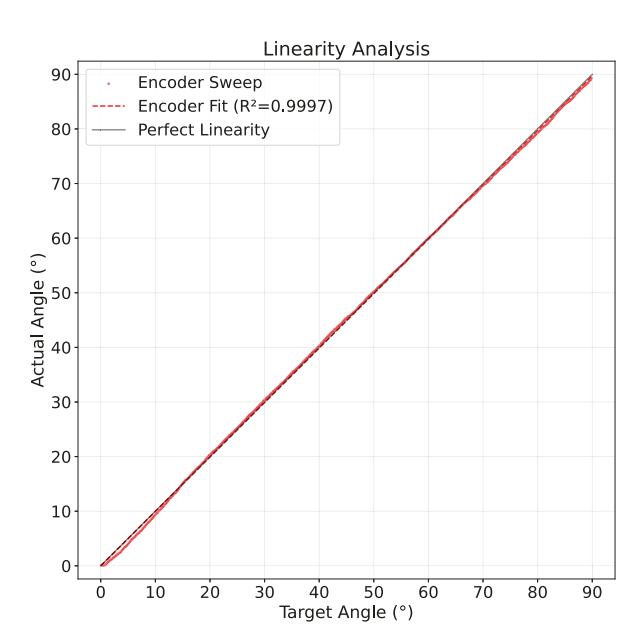


FIG 10. Linearity sweep over 60 s

Table 15 shows the analysis of the tracking accuracy tests

TAB 15. Linearity performance metrics

Metric	Value
R-squared	0.9997
Mean Absolute Error	0.40°
RMS Error	0.47°
Maximum Error	1.10°

4.2.2. Step Tests

Multiple step tests with increasing step size were performed up and down the tilt range to assess the step response and time constant, as well as the angle accuracy when settled. Step sizes up to 10° amplitude showed an average time constant of $0.22\,\mathrm{s}$ with larger steps, the rate constraint is starting to limit the response, and increased time constants and settling times were observed. The 10° step size test is depicted in Figure 11.

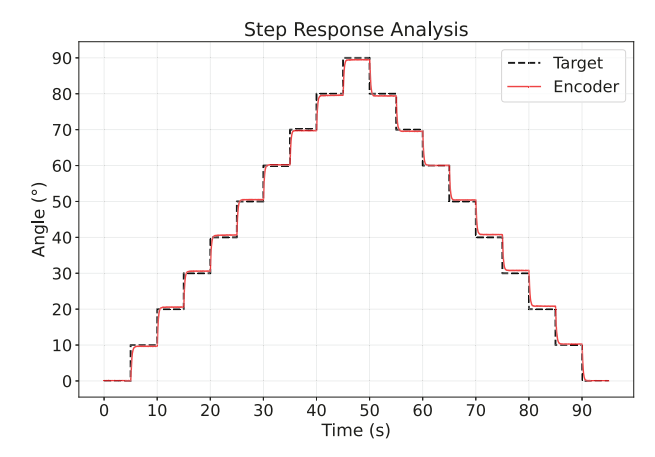


FIG 11. Step response at 10°

In terms of step accuracy, please consult the representative figures in Table 16.

TAB 16. Step accuracy metrics

Metric	Value
Steps	9
Mean Absolute Error	0.46°
Maximum Error	0.85°
Step Accuracy	0.29°
Step Repeatability	0.34°
Time constant (ampl. $<10^{\circ}$)	0.22 s

The tilt time for the full 90° step to settle to within 2% of the final value was measured at $1.52\,\mathrm{s}$, shown in Figure 12, with typical PT1 behavior (3 runs were measured with step up and down times averaged). The average maximum angular tilt speed was measured at $72.6^\circ/\mathrm{s}$, matching expectations. When this rate constraint is reached, which happens above amplitudes of about 10° the time constant starts to increase reaching $0.9\,\mathrm{s}$ for the 90° step.

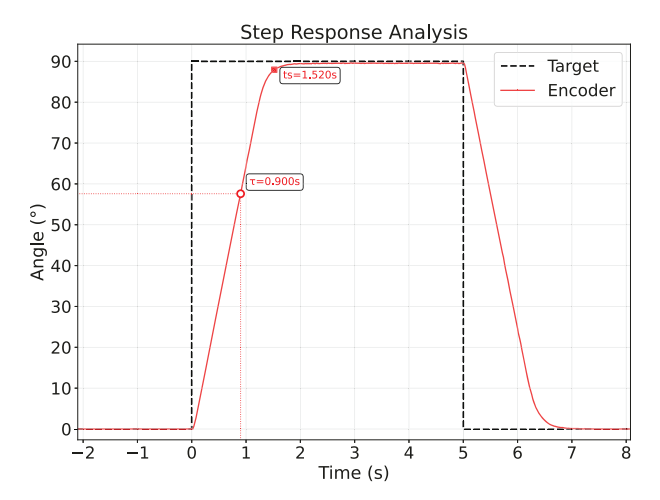


FIG 12. Step response 90°

4.2.3. Hysteresis Tests

Hysteresis tests were also performed assessing the accuracy difference between upwards and downwards movements of the tilt-wing. The Test shown in Figure 13 comprised three movement cycles between 30° and 60° with each cycle taking $60 \, \text{s}$ to perform.

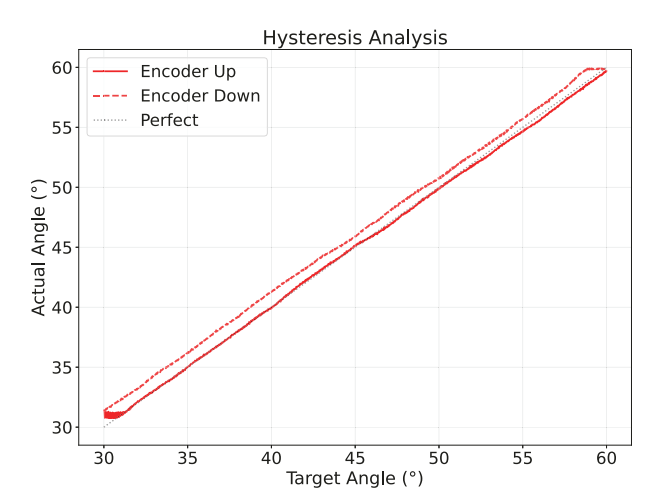


FIG 13. Hysteresis test 15° amplitude

The analysis of the test is provided in Table 17.

TAB 17. Hysteresis analysis metrics

Metric	Value
Analysis range	30.0° to 60.0°
Comparison points	50
Average hysteresis	1.04°
Maximum hysteresis	1.33°
RMS hysteresis	1.07°

4.2.4. Tracking Bandwidth Tests

To assess the tracking bandwidth in Hz of input signal, the amplitude and phase of the tilt angle are measured with increasing sinusoidal input frequencies and with varying angle amplitudes. The cutoff is set at $-3\,\mathrm{dB}$

or -90 $^{\circ}$ phase lag, whichever is reached first. The tests are performed from 0.1 to 5 Hz sine frequency sweep over 30 s duration.

Figure 14 shows the Bode plot of 5° amplitude sine sweep test, showing a 1 Hz tracking bandwidth before hitting the -3 dB limit with a corresponding phase lag of 55.2° .

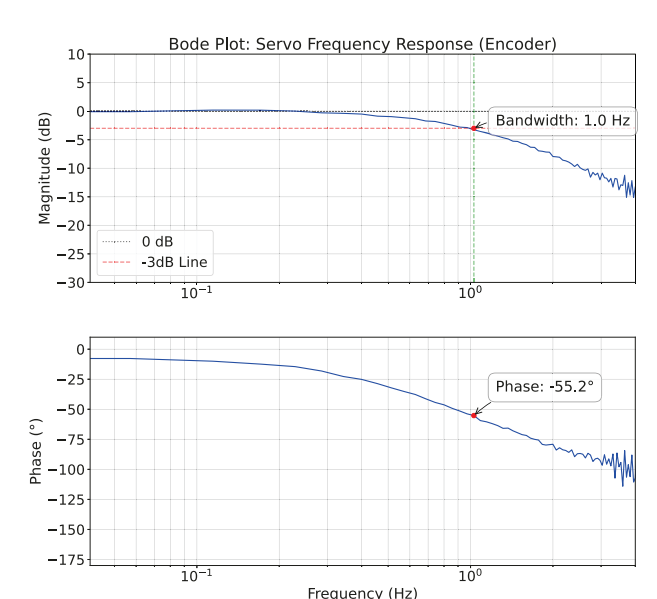


FIG 14. Sine sweep Bode plot 5° amplitude

With a 30° amplitude the test is resulting in a decreased 0.6 Hz tracking bandwidth with 47.7° phase lag. The tracking bandwidth shows the same behavior as the time constant decrease where the rate limit of the actuator angular speed is decreasing performance with higher amplitudes.

5. DISCUSSION

The experimental validation and performance characterization of the developed tilt-wing actuator system enables a comprehensive evaluation of its capabilities against design requirements and identification of key limitations for future implementations.

5.1. Performance Against Requirements

The developed tilt-wing actuator successfully meets and exceeds the established design requirements. With a maximum output torque of 20.8 Nm, the system provides a 54% margin above the required 13.5 Nm for realistic transition scenarios, and a 5% margin above the extreme 19.7 Nm worst-case loading. This conservative approach ensures robust operation across the full transition envelope while accounting for gear losses and dynamic loading effects.

The measured tilt performance of $1.52\,\mathrm{s}$ for a full 90° transition closely matches the predicted $1.7\,\mathrm{s}$ based on gear ratio calculations and data sheet values. This performance enables the aggressive transition profiles identified in our optimal control analysis, supporting outbound transition times of $3.4\,\mathrm{s}$ and inbound transitions of $16.3\,\mathrm{s}$. These capabilities represent a significant improvement over the NASA GL-10's reported transition

limitations [7] and exceeds the 10 s tilt-time requirement of the heavier LA-8 system [8]. The implemented actuators weigh in at 295 g each, combined representing 3.9% of the TANDEMIC's total weight while providing high-speed actuation capability not seen on comparable research aircraft.

The optimized polymer helical gear approach demonstrated substantial benefits, achieving a 2.7 times weight reduction compared to metal spur gear alternatives while enabling more compact packaging. This validates the hypothesis that additive manufacturing's geometric design freedom can unlock performance improvements difficult to achieve with conventional manufacturing methods. The complex geometries required for helical gears with symmetric tooth arrangements would be expensive to manufacture using conventional machining but are readily achievable with FFF 3D printing.

The structural validation demonstrated a failure load of 38.5 Nm, providing a safety factor of 1.7 relative to maximum output torque and 2.7 relative to expected aerodynamic loads. This matches typical aerospace engineering safety requirements and confirms the viability of 3D printed polymer gears for high-load mechanical applications in research aircraft.

The comprehensive dynamic characterization reveals excellent linearity ($R^2 = 0.9997$) with sub-degree accuracy $(0.40^{\circ}$ mean absolute error), indicating highly predictable behavior suitable for model-based control design. The measured time constant of 0.22s for small amplitude commands provides sufficient bandwidth for transition control, while the step accuracy of 0.29° and repeatability of 0.34° is sufficient for our flight control application. However, the hysteresis characteristics (averaging 1.0° for moderate amplitudes) suggest that compensation measures may be beneficial for precise positioning tasks. The tracking bandwidth of 1 Hz for small amplitudes decreases to 0.6 Hz for larger commands, indicating rate-limiting behavior that must be considered in control law design. These characteristics inform our flight dynamics models with quantitative data for achieving robust transition maneuvers while accounting for actuator limitations in the control allocation algorithms.

5.2. Limitations and Critical Assumptions

Several limitations must be acknowledged in the current work. The aerodynamic loading analysis assumes quasisteady conditions and neglects dynamic effects such as gust loading and unsteady transition aerodynamics. Real flight conditions may impose higher instantaneous loads than predicted by the steady-state analysis, though the implemented safety margins should accommodate dynamic amplification.

The comprehensive dynamic characterization presented in this study was conducted under controlled laboratory conditions without external aerodynamic loading. During actual flight operations, particularly in transition regimes, these external loads may affect the servo's ability to maintain position accuracy, and potentially modify the time response characteristics.

The material characterization relies on manufacturer-provided properties. Furthermore FFF printing inherently produces anisotropic structures, and layer adhesion failures could occur under different loading orientations. Long-term durability assessment is limited to literature projections rather than comprehensive fatigue testing under representative loading cycles.

The optimization methodology, while comprehensive in scope, makes several simplifying assumptions regarding gear tooth geometry and contact mechanics. The use of standard design formulas may not fully capture the behavior of polymer materials under the complex stress states present in helical gear contacts.

Temperature effects represent another limitation not fully explored in this study. While the selected materials offer good temperature resistance, the thermal environment during aggressive flight maneuvers, particularly in combination with high actuator loading, could affect material properties and system performance. The relatively low thermal loads expected in the demonstrator application should minimize these concerns, but they warrant consideration for larger-scale implementations.

A further lesson learned was that the Greentec Pro material showed creep and creep crack formation under sustained loading. This is a known limitation of PLA+ like materials that can compromise long-term reliability. The superior creep resistance and toughness characteristics of polycarbonate make it a more suitable choice for parts that are pre loaded.

6. CONCLUSIONS

This study successfully developed and validated a high-performance tilt-wing actuator system that meets the demanding requirements of dynamic transition flight while leveraging cost-effective additive manufacturing and COTS components.

6.1. Key Achievements

The key achievements include:

- Development of a servo-driven actuator system providing 20.8 Nm output torque with a 1.52 s tilt time, enabling experiments of aggressive transition maneuvers.
- Comprehensive optimization methodology yielding gear designs that achieve up to a 2.7 times weight reduction compared to conventional spur gear alternatives while maintaining structural integrity.
- Experimental validation of 3D printed helical gears under high loading conditions, demonstrating safety factors of 1.7 relative to operational loads.
- Quantitative assessment of actuator performance impact on transition capability, showing that an actuator powered by a COTS RC-servo with an 8:1 gear ratio enables outbound transitions in 3.4 s and inbound transitions in 16.3 s.
- Comprehensive characterization of the completed actuator system, including tracking accuracy, step response, hysteresis, and tracking bandwidth data, pro-

viding other research teams with validated performance metrics for controller and hardware design.

6.2. Methodological Contributions

The integrated approach developed in this work provides several transferable methodological contributions to the eVTOL development community:

- A systematic framework for deriving actuator requirements from vehicle-level transition performance objectives using optimal control methods
- Multi-material, multi-configuration gear optimization methodology specifically adapted for additive manufacturing constraints
- Comprehensive experimental validation protocol for 3D printed mechanical components under representative operational loading

These methodological advances enable other research teams to adapt the approach to different vehicle configurations, loading conditions, and performance requirements while maintaining confidence in the resulting designs.

6.3. Future Work

Several areas warrant continued investigation to further advance the state of the art in eVTOL actuation systems: **Implementation of optimized design** should prioritize the single-stage polycarbonate (PC) configuration identified through this optimization study.

Extended durability assessment should include comprehensive fatigue testing under representative flight loading profiles.

Flight test validation of the actuator system in the TANDEMIC demonstrator will provide critical data on real-world performance, including dynamic loading effects, thermal behavior, vibration environment effects, and challenges not fully captured in bench testing.

Scaling studies examining the applicability of this approach to larger vehicle classes and higher power requirements would establish the boundaries of the methodology's utility in practical eVTOL development.

The successful development and validation of this actuator system demonstrates that sophisticated mechanical components can be rapidly prototyped and deployed using modern additive manufacturing technologies combined with rigorous engineering analysis.

Contact address:

leo.ott@dlr.de

References

- [1] Johnny T. Doo, Marilena D. Pavel, Arnaud Didey, Craig Hange, Nathan P. Diller, Michael A. Tsairides, Michael Smith, Edward Bennet, Michael Bromfield, and Jessie Mooberry. Nasa electric vertical takeoff and landing (evtol) aircraft technology for public services a white paper. White paper, National Aeronautics and Space Administration, Aug. 2021. [Online]. Available: https://ntrs.nasa.gov/citation s/20205000636 [accessed Aug. 18, 2025].
- [2] R Goyal, Colleen Reiche, Chris Fernando, Jacquie Serrao, Shawn Kimmel, Adam Cohen, and Susan Shaheen. Urban air mobility (uam) market study. Technical report, National Aeronautics and Space Administration, Washington, D.C., Nov. 2018. [Online]. Available: https://ntrs.nasa.gov/citations/20190001472 [accessed Aug. 18, 2025].
- [3] Martin D. Maisel, Demo J. Giulianetti, and Daniel C. Dugan. The history of the xv-15 tilt rotor research aircraft: From concept to flight, Mar. 2000. [Online]. Available: https://ntrs.nasa.gov/ci tations/20000027499 [accessed Aug. 18, 2025].
- [4] Marc May, Daniel Milz, and Gertjan Looye. Semiempirical aerodynamic modeling approach for tandem tilt-wing evtol control design applications. In AIAA SciTech 2023 Forum, National Harbor, MD, US, Jan. 2023. DOI: 10.2514/6.2023-1529.
- [5] Daniel Milz, Marc May, and Gertjan Looye. Dynamic inversion-based control design for multi-phase tandem tilt-wing flight. 01 2025. DOI: 10.2514/6.2025-2698.
- [6] Marc May, Daniel Milz, and Gertjan Looye. Towards the determination of the dynamic transition corridor for tandem tilt-wing aircraft. 08 2024. DOI: 10.2514/6.2024-4417.
- [7] Robert G. McSwain, Louis J. Glaab, Colin R. Theodore, Ray D. Rhew, and David D. North. Greased lightning (gl-10) performance flight research flight data report. Technical report, National Aeronautics and Space Administration, Nov. 2017. [Online]. Available: https://ntrs.nasa.gov/citations/20180000765 [accessed Aug. 18, 2025].
- [8] Robert G. McSwain, Steven C. Geuther, Gregory Howland, Michael D. Patterson, Siena K. Whiteside, David D. North, Louis J. Glaab, and Ray D. Rhew. An experimental approach to a rapid propulsion and aeronautics concepts testbed. Technical report, National Aeronautics and Space Administration, Langley Research Center, Hampton, Virginia, Jan. 2020. [Online]. Available: https://ntrs.nasa.go v/citations/20200000698 [accessed Aug. 18, 2025].
- [9] David D. North, Ronald C. Busan, and Greg Howland. Design and fabrication of the langley aerodrome no. 8 - distributed electric propulsion vtol testbed. In AIAA Scitech 2021 Forum, Nov. 2020.

- [Online]. Available: https://ntrs.nasa.gov/citations/20205010035 [accessed Aug. 18, 2025].
- [10] E. Cetinsoy, S. Dikyar, C. Hancer, Kaan Oner, Efe Sirimoglu, Mustafa Unel, and Mahmut Aksit. Design and construction of a novel quad tiltwing uav. *Mechatronics*, 22:723745, Sep. 2012. DOI: 10.1016/j.mechatronics.2012.03.003.
- [11] G.D. Goh, S. Agarwala, G.L. Goh, V. Dikshit, S.L. Sing, and W.Y. Yeong. Additive manufacturing in unmanned aerial vehicles (uavs): Challenges and potential. *Aerospace Science and Technology*, 63:140–151, 2017. ISSN:1270-9638. DOI: 10.1016/j.ast.2016.12.019.
- [12] Dale Satran and M.H. Snyder. Two dimensional tests of ga(w)-1 and ga(w)-2 airfoils at angles- of attack from 0 to 360 degrees. Technical report, Wichita State University, Wichita, Kan, US, Jan 1977. [Online]. Available: https://soar.wichita.edu/bitstream/handle/10057/5692/WER-1.pdf?sequence= 5 [accessed Aug. 18, 2025].
- [13] Ziqing Ma, Ewoud J.J. Smeur, and Guido C.H.E. de Croon. Wind tunnel tests of a wing at all angles of attack. *International Journal of Micro Air Vehicles*, 14, 2022. DOI: 10.1177/17568293221110931.
- [14] Y. Dobrev, T. Ostermann, J. Holsten, and D. Moormann. Investigation of the effects of propeller slipstream and tilt angle on the control device effectiveness of a tiltwing aircraft. In *Proceedings of the Deutscher Luft-und Raumfahrtkongress 2012, Berlin*, page 8, Bonn, Feb. 2015. Deutsche Gesellschaft für Luft-und Raumfahrt Lilienthal-Oberth e.V. URN: urn:nbn:de:101:1-2015020615969.
- [15] Hermann Schlichting and Erich Truckenbrodt. Aerodynamik des Flugzeuges. Klassiker der Technik. Springer Berlin, Heidelberg, Berlin, Heidelberg, 3 edition, 2000. ISBN: 978-3-540-67375-0. Originally published as a monograph. DOI: 10.1007/978-3-642-56910-4.
- [16] W. H. Wentz, H. C. Seetharam, and K. A. Fiscko. Force and pressure tests of the ga(w)-1 airfoil with a 20% aileron and pressure tests with a 30% fowler flap. Technical report, Wichita State University, Wichita, Kan, US, Jun. 1977. [Online]. Available: https://ntrs.nasa.gov/citations/19770018139 [accessed Aug. 18, 2025].
- [17] Benjamin M. Simmons. Efficient variable-pitch propeller aerodynamic model development for vectored-thrust evtol aircraft. In AIAA AVIATION 2022 Forum, 2022. DOI: 10.2514/6.2022-3817.
- [18] Benjamin Simmons and David Hatke. Investigation of high incidence angle propeller aerodynamics for subscale evtol aircraft. Technical report, 05 2021. [Online]. Available: https://ntrs.nasa.gov/citation s/20210014010 [accessed Aug. 18, 2025].

- [19] Marc S. May, Daniel Milz, and Gertjan Looye. Transition Strategies for Tilt-Wing Aircraft. DOI: 10.2514/6.2024-1289.
- [20] Hans-Jörg Dennig, Livia Zumofen, and Andreas Kirchheim. Feasibility investigation of gears manufactured by fused filament fabrication. In Mirko Meboldt and Christoph Klahn, editors, *Industrializ*ing Additive Manufacturing, pages 304–320, Cham, 2021. Springer International Publishing. ISBN: 978-3-030-54334-1.
- [21] Mert Tunalioglu and Bekir Agca. Wear and service life of 3-d printed polymeric gears. *Polymers*, 14:2064, May 2022. DOI: 10.3390/polym14102064.
- [22] Blanca Boado-Cuartero, Javier Pérez-Álvarez, and Elena Roibás-Millán. Material characterization of high-performance polymers for additive manufacturing (am) in aerospace mechanical design. *Aerospace*, 11(9), 2024. ISSN: 2226-4310. DOI: 10.3390/aerospace11090748.
- [23] Hubert Hinzen. 2 Lager, Welle-Nabe-Verbindungen, Getriebe. De Gruyter Oldenbourg, Berlin, Boston, 2022. ISBN: 9783110747072. DOI: doi:10.1515/9783110747072.
- [24] E. J. Hearn. *Mechanics of Materials: An Introduction to the Mechanics of Elastic and Plastic Deformation of Solids and Structural Components.* Elsevier Science & Technology, 1985.

APPENDIX

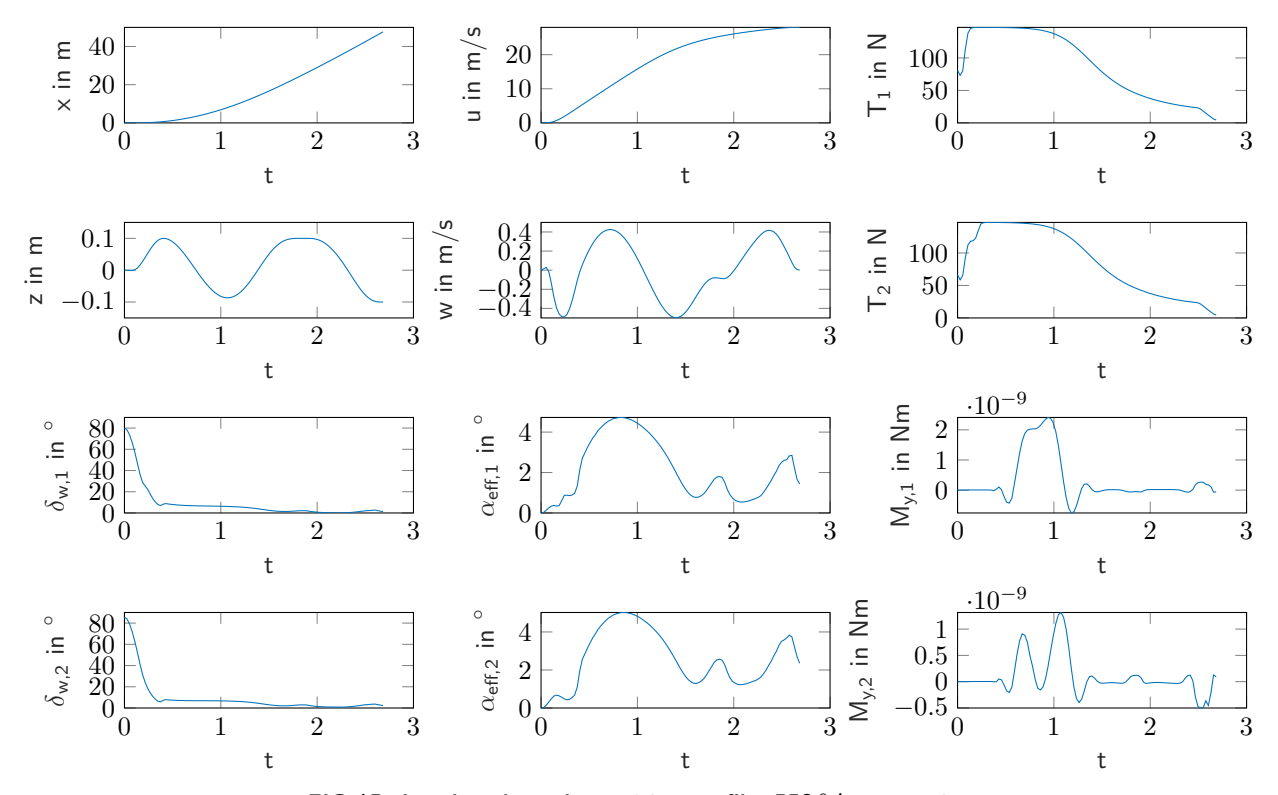


FIG 15. Level outbound transition profile, 550 $^{\circ}$ /s constraint

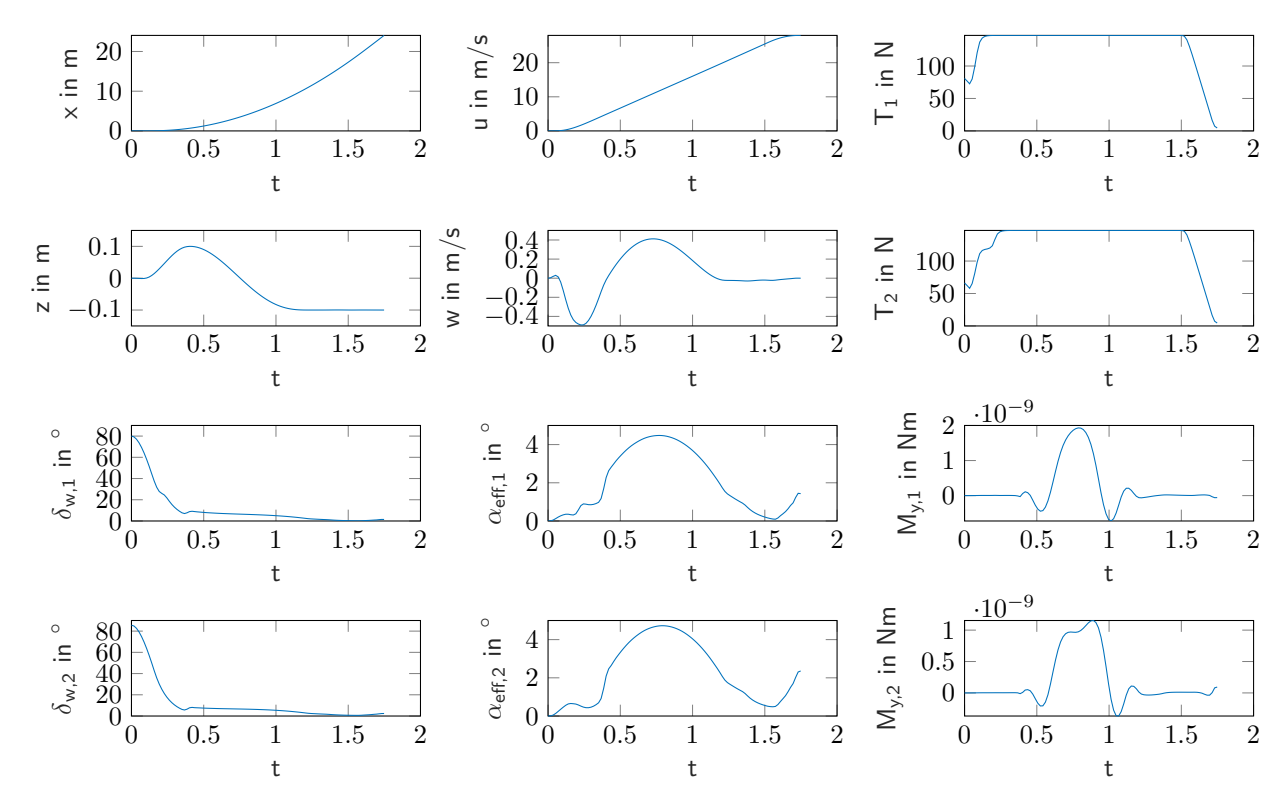


FIG 16. Level outbound transition profile, 550 $^{\circ}/\text{s}$ constraint, no thrust decline

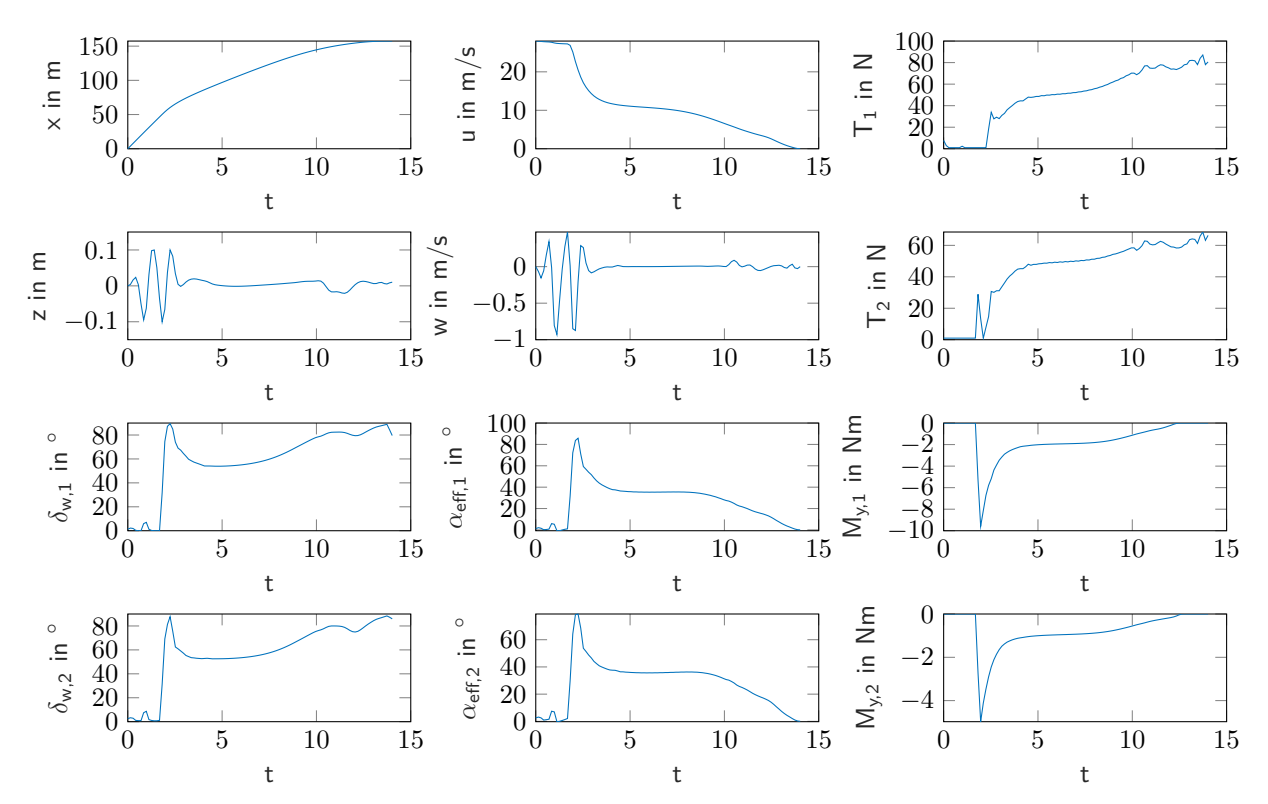


FIG 17. Level inbound transition profile (cruise to hover), 550 $^{\circ}$ /s constraint

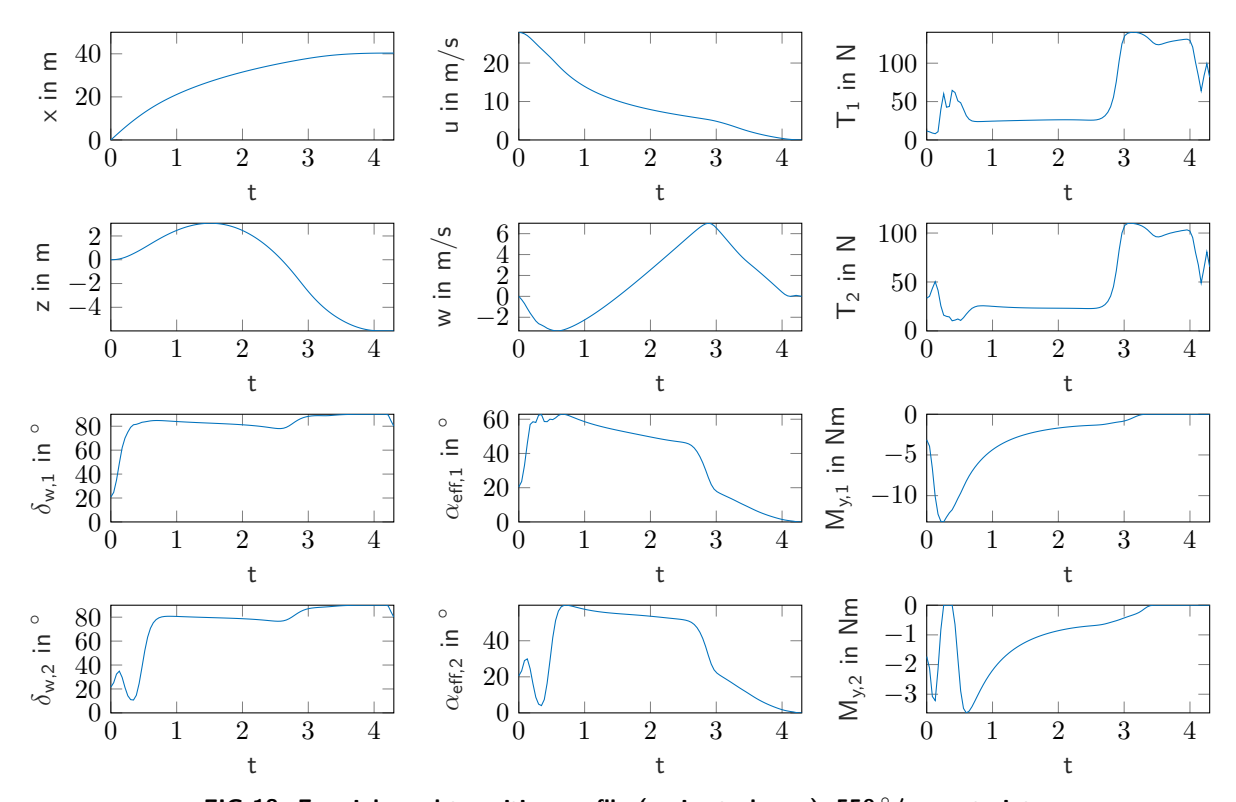


FIG 18. Free inbound transition profile (cruise to hover), 550 $^{\circ}/s$ constraint

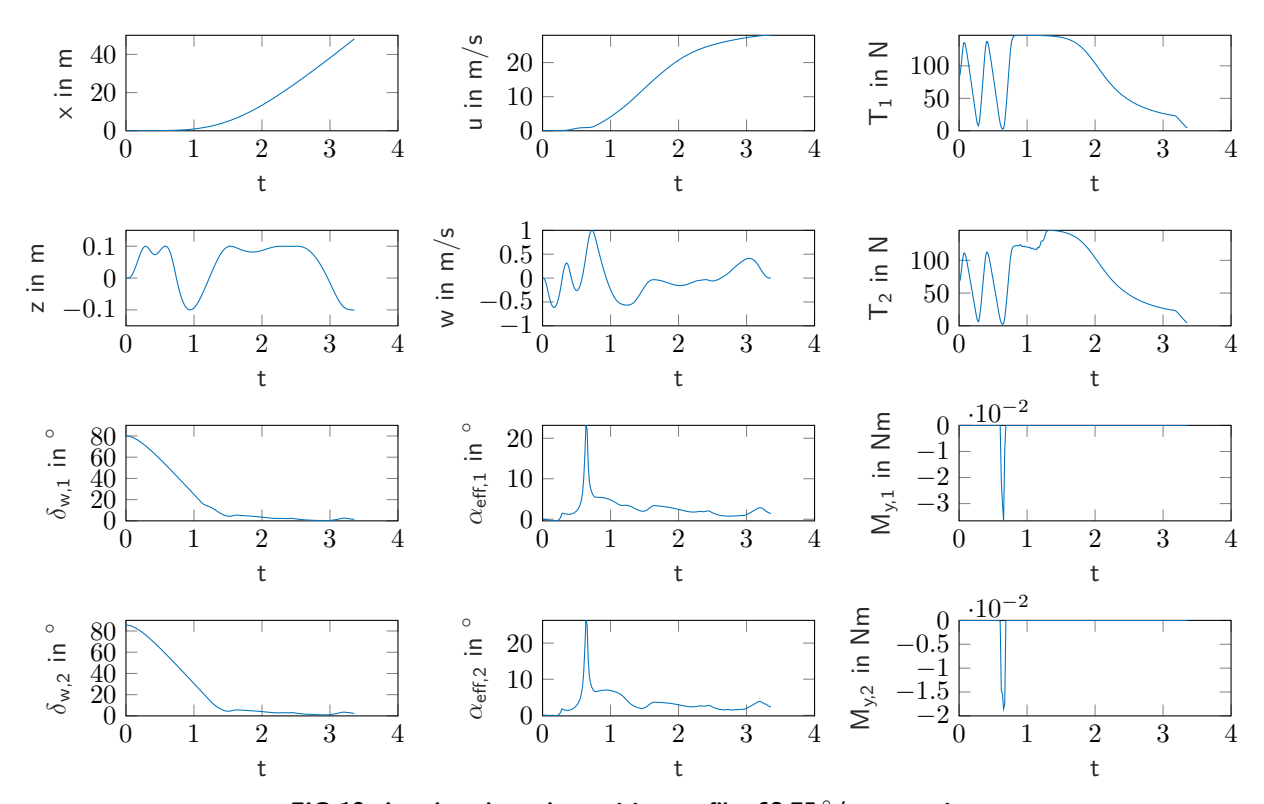


FIG 19. Level outbound transition profile, 68.75 $^{\circ}/s$ constraint

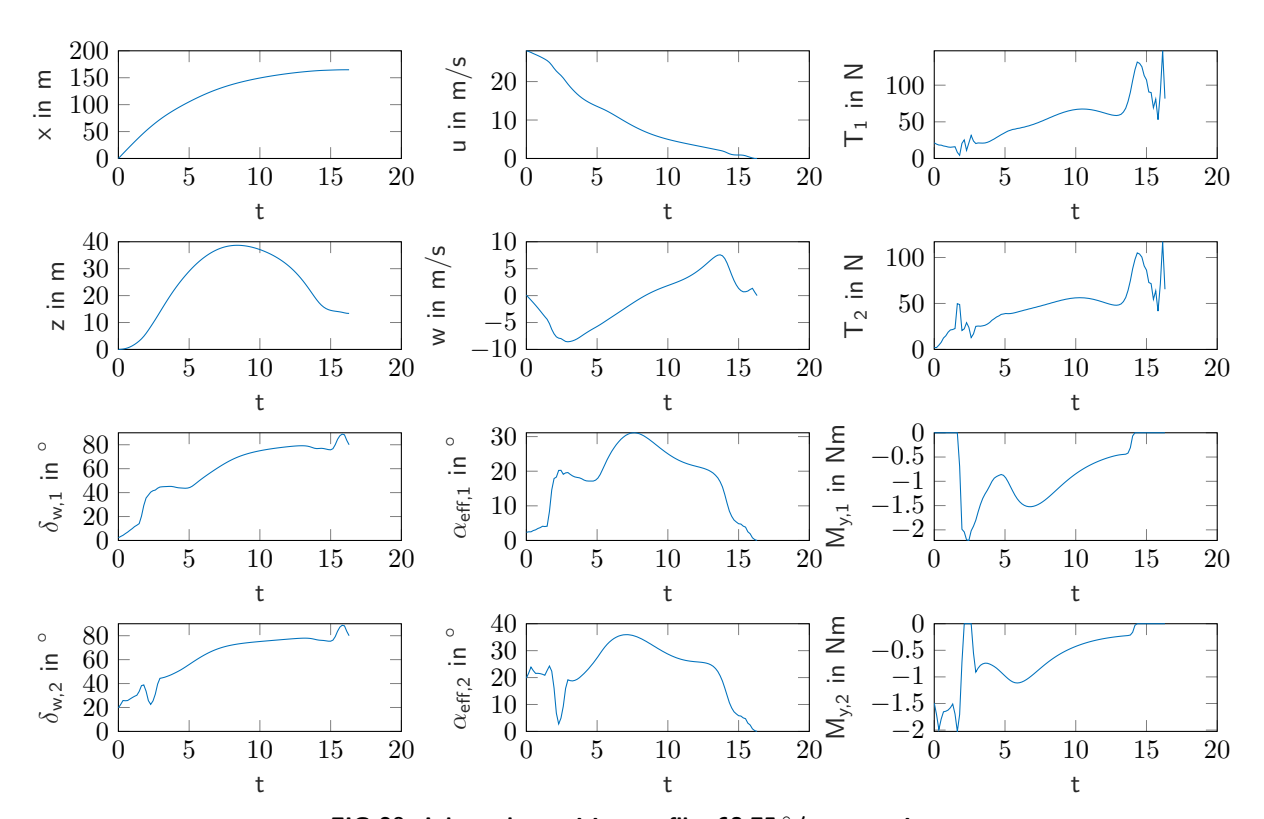


FIG 20. Inbound transition profile, 68.75 $^{\circ}/s$ constraint

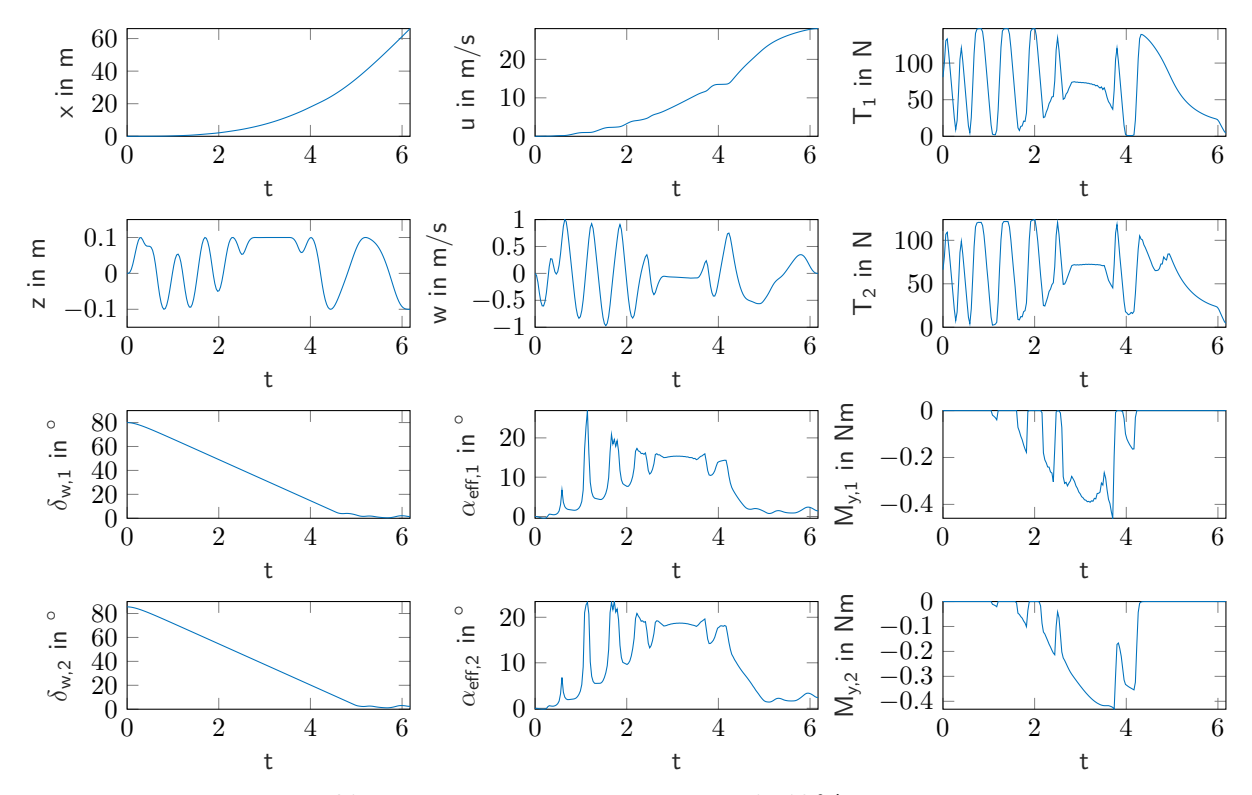


FIG 21. Level outbound transition profile, 17.19 $^{\circ}$ /s constraint

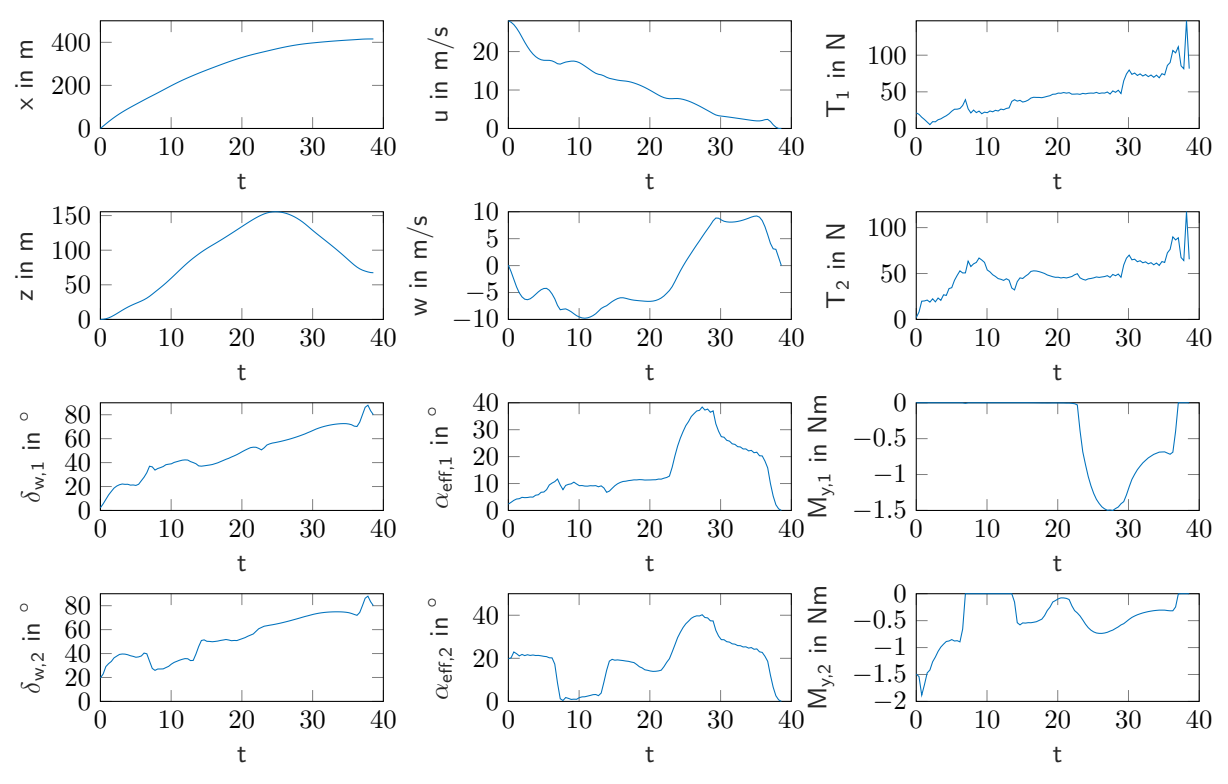


FIG 22. Inbound transition profile, $17.19^{\circ}/s$ constraint

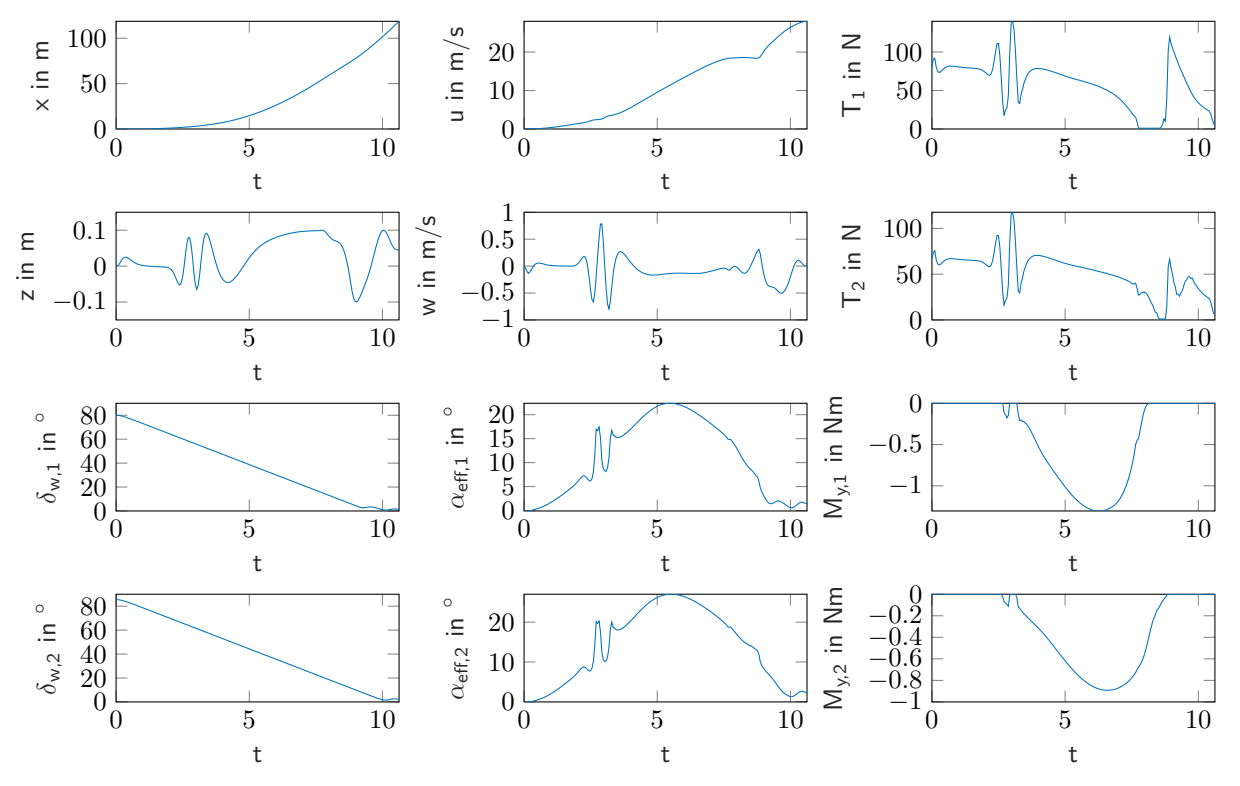


FIG 23. Level outbound transition profile, $8.59^{\circ}/s$ constraint

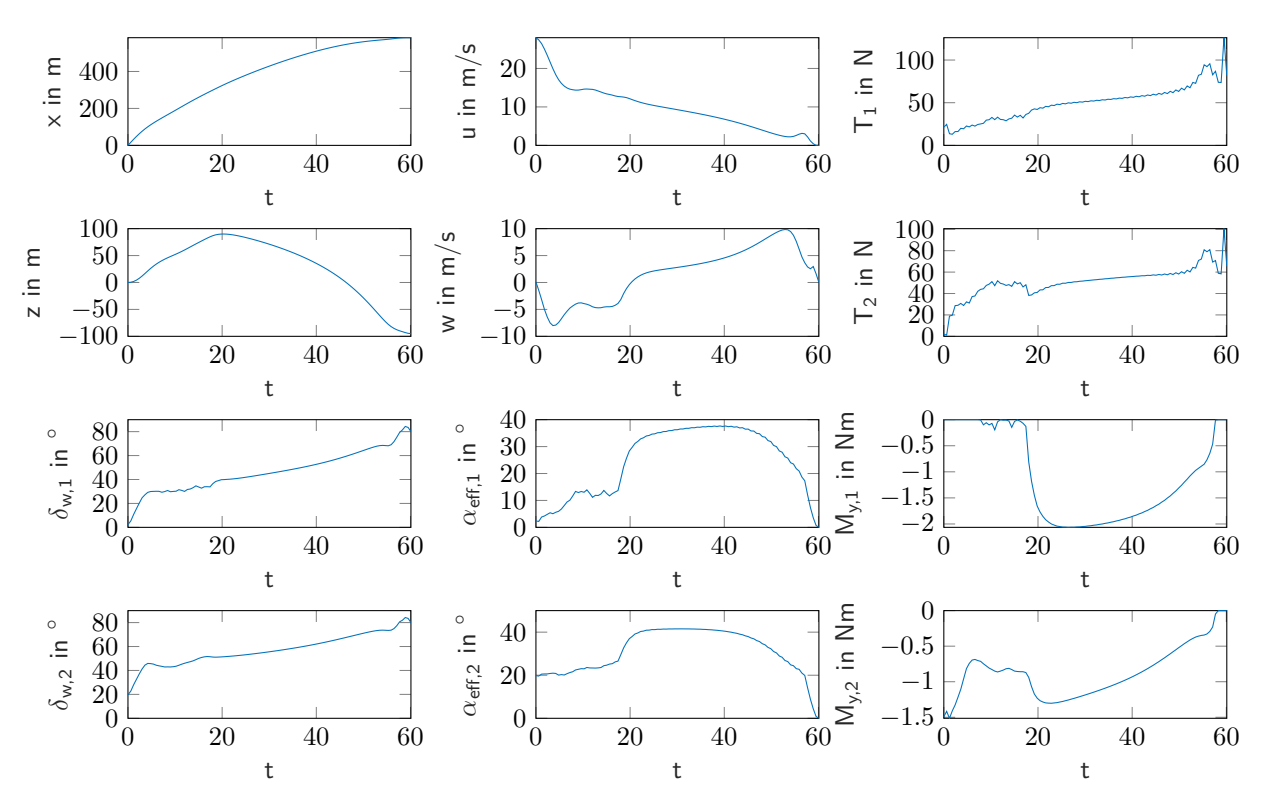


FIG 24. Inbound transition profile, 8.59 °/s constraint